Research Article

Journal of Environmental Nanotechnology

# Green-synthesized $ZrO_2$ Nanoparticles for Congo Red Adsorption: Machine Learning Prediction and Multi-criteria Optimization

V. Bhanu Rekha[1], V. Ratha[2], V. Anitha[3], M. A. Mukunthan[4], V. Seedha Devi[5] and A. Jose Anand[6*]

[1]Department of Fashion Designing, SRM Institute of Science and Technology Ramapuram Campus, Chennai, TN, India
[2]Department of Management Studies, Jaya Engineering College, Thiruniravur, Tiruvallur, TN, India
[3]Department of Electronics and Communication Engineering, Sri Muthukumaran Institute of Technology, Chikkarayapuram, Chennai, TN, India
[4]Department of Computer Science and Engineering, Vel Tech Rangarajan Dr. Sagunthala R&D Institute of Science and Technology, Avadi, Thiruvallur, TN, India
[5]Department of Information Technology, Jaya Engineering College, Thiruninravur, Tiruvallur, TN, India
[6]Department of Electronics and Communication Engineering, KCG College of Technology, Karapakkam, Chennai, TN, India
Received: 31.07.2026 Accepted: 09.08.2026 Published: xx.xx.xxxx
*joseanand97@gmail.com

## ABSTRACT

Zirconium dioxide ($ZrO_2$) nanoparticles were synthesized from zirconyl chloride octahydrate using *Toddalia asiatica* leaf extract through an environmentally sustainable route and evaluated for Congo Red (CR) adsorption. XRD, FTIR, SEM–EDX, TGA, and XRF analyses confirmed the crystalline structure, morphology, surface functional groups, elemental composition, and thermal stability of the synthesized nanoparticles. Adsorption performance was investigated using an integrated Taguchi–ANOVA–PSI–PIV–CFANN framework. ANOVA revealed that $ZrO_2$ dosage predominantly influenced CR removal, whereas initial concentration and dosage governed adsorption capacity. PSI–PIV identified Run 27 at 75 mg $L^{-1}$ CR, 90 min, 40 °C and 0.25 g $L^{-1}$ $ZrO_2$ as the best experimental compromise, achieving 63.56% removal efficiency and the experimentally calculated adsorption capacity. CFANN–PSI–PIV predicted an optimum at 75 mg $L^{-1}$, 90 min, 50 °C, and 0.25 g $L^{-1}$, with 67.2169% removal efficiency and the corresponding predicted adsorption capacity. The latter condition represents a model-predicted optimum. These findings demonstrate that green-synthesized $ZrO_2$ nanoparticles, combined with data-driven optimization, offer a promising approach for treating CR-contaminated wastewater.

**Keywords:** Green synthesis; Optimization; Adsorption; Thermal stability; Crystalline structure.

## 1. INTRODUCTION

Industrial expansion, rapid urbanization, and population growth have intensified pressure on freshwater resources while increasing the discharge of complex contaminants into aquatic environments. Heavy metals released from electroplating operations are persistent, non-biodegradable, and capable of accumulating in living organisms, thereby creating serious ecological and human-health risks (Rao *et al.* 2025). Chromium-bearing tannery effluent is similarly hazardous and demands efficient, regenerable, and environmentally benign treatment technologies that minimize secondary pollution (Sharmiladevi *et al.* 2024). Sustainable urban wastewater management therefore requires a transition from the conventional linear "take–make–waste" model to closed-loop systems integrating water conservation, wastewater reclamation, resource recovery, and treated-water reuse (Varma *et al.* 2024).

Synthetic dyes and pharmaceutical residues constitute another critical class of aquatic pollutants because of their chemical stability, intense colour, toxicity, and resistance to conventional biological treatment. Green catalytic processes offer an economical and environmentally sustainable route for rapidly degrading persistent organic dyes in wastewater (Amale *et al.* 2026). Sunlight-driven photocatalysis is particularly advantageous because it utilizes renewable solar energy to generate ROS capable of decomposing complex pollutants into less harmful products. Such treatment can reduce the residual toxicity of dye-containing wastewater and facilitate its safe reuse in agricultural and environmental applications (Mungle *et al.* 2026).

Among metal-oxide photocatalysts, $ZrO_2$ has attracted considerable attention owing to its physicochemical stability, low toxicity, favourable surface chemistry, and resistance to chemical and thermal degradation. Nevertheless, its wide bandgap and rapid electron–hole recombination can restrict photocatalytic performance under visible light. Green synthesis, heterojunction construction, metal-ion doping,

carbonaceous support incorporation, and polymer immobilization have therefore been employed to improve surface area, visible-light absorption, charge separation, adsorption capacity, and catalyst recovery.

Green-synthesized $ZrO_2$ nanoparticles prepared using zirconyl oxychloride and aqueous *Toddalia asiatica* leaf extract degraded more than 95% of methylene blue under sunlight, confirming their potential for dye-contaminated wastewater treatment (Kathirvel *et al.* 2025). Chitosan microcapsules containing *Toddalia asiatica* extract demonstrated favourable functional stability and provided a sustainable bio-based platform for environmentally responsible material development (Zhu *et al.* 2024a). Urea–formaldehyde resin microcapsules loaded with the same extract exhibited improved stability and chemical resistance, further demonstrating the functional potential of plant-derived components in environmental materials (Zhu *et al.* 2024b).

Plant-mediated synthesis has also been applied to produce $ZrO_2$ nanoparticles for pharmaceutical and dye removal. $ZrO_2$ nanoparticles synthesized using *Cycas revoluta* leaf extract achieved 60.81% doxycycline removal under optimized conditions, with a Langmuir maximum adsorption capacity of 11.276 mg $g^{-1}$ (Sharma *et al.* 2026). *Ficus carica* fruit extract-mediated $ZrO_2$ nanoparticles exhibited spherical morphology, particle sizes of 20–35 nm, and a BET surface area of 83.5 $m^2$ $g^{-1}$. These nanoparticles degraded 98% of methylene blue and 94% of Rhodamine B within 90 min and retained more than 95% of their initial activity after three cycles (Rajeswaran *et al.* 2026). Similarly, *Raphanus sativus* leaf-mediated $ZrO_2$ nanoparticles achieved 78% metronidazole degradation under basic conditions and 57% nifedipine degradation under acidic conditions, demonstrating their applicability to pharmaceutical-contaminated wastewater (Rana *et al.* 2026).

Surface modification and composite formation can further enhance the treatment performance of $ZrO_2$. Ag-doped $ZrO_2$ with mixed tetragonal–monoclinic phases achieved 95% Rhodamine B degradation within 150 min under visible light, compared with only 59% for pure $ZrO_2$, while maintaining good catalytic reusability (Li *et al.* 2026). A $Te^{4+}/Er^{3+}$-doped $ZrO_2$ photocatalyst attained 99% Congo Red degradation and 79.9% total organic carbon removal within 100 min and retained 96.4% degradation efficiency after four cycles (Halder *et al.* 2024). The $ZrO_2$–chitosan hybrid composite achieved visible-light degradation efficiencies of 91.11%, 69.11%, and 78.40% for Methyl Orange, Congo Red, and 4-hydroxybenzoic acid, respectively (Das *et al.* 2022).

Combining $ZrO_2$ with other semiconductors suppresses photogenerated electron–hole recombination and promotes interfacial charge transfer. Electrospun Zr/Ag-co-doped $TiO_2$ nanofibres exhibited a pseudo-first-order rate constant of 0.0405 $min^{-1}$ for Congo Red degradation, approximately 12 times greater than that of pure $TiO_2$ nanofibres (Qi *et al.* 2021). Microwave-synthesized $ZrO_2$/ZnO heterostructures degraded 87% of Congo Red and 98% of methylene blue within 60 min under sunlight and remained stable over three cycles (Wahba and Yakout, 2022). Recyclable CuO–$ZrO_2$@PAN nanofibre mats achieved more than 96% methylene blue, approximately 90% Congo Red, 85% Bismarck Brown, and 75% Reactive Black removal within 60 min, demonstrating their potential as recoverable photoactive filtration materials (Rajput *et al.* 2026). More recently, (Sismanoglu and Buran, 2025) investigated Congo Red adsorption using $ZrO_2$ and olive-pulp/$ZrO_2$ adsorbents, reporting a Langmuir capacity of 13 mg $g^{-1}$ for $ZrO_2$ and 46–84 mg $g^{-1}$ for the corresponding composite systems at 45 °C.

Adsorption–photocatalysis integration provides an additional route for improving pollutant capture and degradation. An alkali-activated Indian bael-shell biochar/$ZrO_2$ composite exhibited a mesoporous structure and maximum malachite green adsorption capacity of 96.62 mg $g^{-1}$. Its adsorption followed pseudo-second-order kinetics and the Langmuir isotherm, while its removal efficiency remained at 84.63% after five reuse cycles (Paul *et al.* 2026). Morphological and elemental analyses of PVA/$ZrO_2$-based nanocomposites further confirmed that $ZrO_2$ can be successfully incorporated into polymeric matrices, supporting the development of stable and recoverable materials for wastewater treatment (Senthilkumar *et al.* 2026).

This study investigates the green synthesis of zirconium dioxide nanoparticles using zirconyl chloride octahydrate and *Toddalia asiatica* leaf extract for Congo Red (CR) adsorption. Plant-derived phytochemicals facilitate nanoparticle formation and provide an environmentally compatible alternative to conventional synthesis methods. Adsorption performance was examined by varying $ZrO_2$ dosage, contact time, initial CR concentration and temperature according to a Taguchi L27 design. ANOVA was employed to determine the significance and contribution of all variables. PSI and PIV methods were integrated to assign objective response weights and identify the best compromise between adsorption capacity and CR removal efficiency. A cascade-forward artificial neural network was developed for nonlinear response prediction. The synthesized nanoparticles were characterized using XRD, FTIR, SEM–EDX, TGA/DTA and XRF. Previous $ZrO_2$ adsorption studies have generally investigated experimental optimization, statistical analysis, multi-criteria ranking, or machine-learning prediction separately. The novelty of the present study lies in integrating Taguchi L27 design, ANOVA, objective PSI weighting, PIV multi-response ranking, and a 4–8–2 CFANN within a unified framework for simultaneous prediction and optimization of Congo Red removal

Article in Press

efficiency and adsorption capacity. The integrated framework demonstrates the applicability of green-synthesized $ZrO_2$ NPs for treating CR-contaminated wastewater.

## 2. MATERIALS AND METHODOLOGY

### 2.1 Chemicals and Plant Materials

Analytical-grade zirconyl chloride octahydrate ($ZrOCl_2 \cdot 8H_2O$, ≥99.85%) was used as the zirconium source without additional purification. Fresh *Toddalia asiatica* leaves were collected and processed for aqueous extract preparation. Double-distilled water was employed throughout nanoparticle synthesis and adsorption experiments. Congo Red (CR), a water-soluble anionic azo dye widely associated with textile effluents, was selected as the target contaminant for evaluating the adsorption performance of the synthesized $ZrO_2$ nanoparticles.

### 2.2 Characterization of $ZrO_2$ Nanoparticles

The crystalline phase of the synthesized $ZrO_2$ nanoparticles was examined using an Empyrean X-ray diffractometer with Cu Kα radiation. Chemical bonding and functional groups were evaluated over 4000–400 $cm^{-1}$ using a Thermo Scientific Nicolet iS50 FTIR spectrometer with KBr pellets. Surface morphology and elemental composition were investigated using a ZEISS GeminiSEM 360 equipped with an EDX detector at an accelerating voltage of 10 kV. Elemental oxide composition was determined using an Epsilon 1 XRF spectrometer. Thermal behaviour was evaluated using a NETZSCH STA 449 F3 thermal analyser. Samples were heated from 25 to 1000 °C in alumina crucibles at 10 °C $min^{-1}$ at an airflow of 40 mL $min^{-1}$. Optical absorption was recorded using a Shimadzu UV-2600i spectrophotometer. These analyses established the structural, functional, morphological, elemental, thermal and optical characteristics of the prepared $ZrO_2$ nanoparticles.

### 2.3 Preparation of *Toddalia asiatica* Extract

Fresh *Toddalia asiatica* leaves were thoroughly rinsed with deionized water and shade-dried to constant mass. Dried material was ground using a Retsch ZM 200 mill and passed through a 125 µm sieve. Subsequently, 10 g of leaf powder was dispersed in 100 mL of double-distilled water and heated at 60 °C for 30 minutes using an IKA C-MAG HS 7 hotplate stirrer. After cooling, the mixture was centrifuged at 5000 rpm using a REMI R-8C centrifuge. The clarified supernatant was collected and stored at 4 °C until nanoparticle synthesis.

### 2.4 Green Synthesis of $ZrO_2$ Nanoparticles

$ZrO_2$ nanoparticles were synthesized using *Toddalia asiatica* leaf extract. A 0.1 M zirconyl chloride octahydrate ($ZrOCl_2 \cdot 8H_2O$) solution was gradually added to the filtered plant extract under continuous stirring. The reaction mixture was maintained at 80 °C for 4 h. The resulting precipitate was recovered and repeatedly washed with double-distilled water and ethanol to remove residual ions and organic impurities. The washed product was dried at 80 °C and subsequently calcined at 500 °C for 3 h. The obtained $ZrO_2$ nanoparticles were cooled and stored in a desiccator until further characterization and adsorption experiments. During heating, phytochemicals in the extract promoted precursor hydrolysis, complexation, and stabilization, resulting in the formation of a pale precipitate. Likewise, $ZrO_2$ nanoparticles green-synthesized using *Anisomeles malabarica* leaf extract exhibited mixed monoclinic–tetragonal phases and enhanced photocatalytic activity (Nadesan *et al.* 2026). Final powder was cooled and stored in a desiccator.

The simplified formation reactions are expressed as:

$$ZrOCl_2 + 3H_2O \rightarrow Zr(OH)_4 + 2HCl \quad \ldots (1)$$

$$Zr(OH)_4 \xrightarrow{\Delta} ZrO_2 + 2H_2O \quad \ldots (2)$$

### 2.5 Preparation of Congo Red Solutions

Congo Red (CR), an anionic diazo dye with formula $C_{32}H_{22}N_6Na_2O_6S_2$, was selected as the adsorbate. It had a molar mass of 696.66 g $mol^{-1}$ and a maximum absorption wavelength of approximately 497 nm. The stock solution was prepared by dissolving an accurately weighed quantity of CR in double-distilled water. Working solutions of 25, 50 and 75 mg $L^{-1}$ were subsequently prepared through appropriate dilution.

### 2.6 Batch Adsorption Experiments

Batch adsorption experiments were performed using 50 mL of Congo Red solution in 250 mL thermostatic flasks at 300 rpm. The investigated variables were initial CR concentration of 25, 50, and 75 mg $L^{-1}$, contact time of 30, 60, and 90 min, temperature of 30, 40, and 50 °C, and $ZrO_2$ dosage of 0.25, 0.50, and 0.75 g $L^{-1}$. After the prescribed contact period, the nanoparticles were separated by filtration, and the residual CR concentration was measured spectrophotometrically at 497 nm. Each adsorption condition was performed in [n=3] independent replicates, and the reported responses represent the mean of these measurements.

Removal efficiency and equilibrium adsorption capacity was calculated as:

$$R(\%) = \frac{C_0 - C_e}{C_0} \times 100 \quad \ldots (3)$$

Article in Press

$$q_e = \frac{(C_0 - C_e)V}{m} \quad \ldots (4)$$

where $C_0$ and $C_e$ were initial and equilibrium CR concentrations $(\mathrm{mgL^{-1}})$, $V$ were solution volume (L), and $m$ were $ZrO_2$ mass (g

## 2.7 Taguchi Experimental Design

A Taguchi L27 OA was employed to study four adsorption variables at three levels while reducing the number of experimental combinations. The control factors were initial Congo Red concentration, contact time, temperature, and $ZrO_2$ nanoparticle dose. Equilibrium adsorption capacity and Congo Red removal efficiency were selected as two performance responses, and both were treated as larger-the-better characteristics.

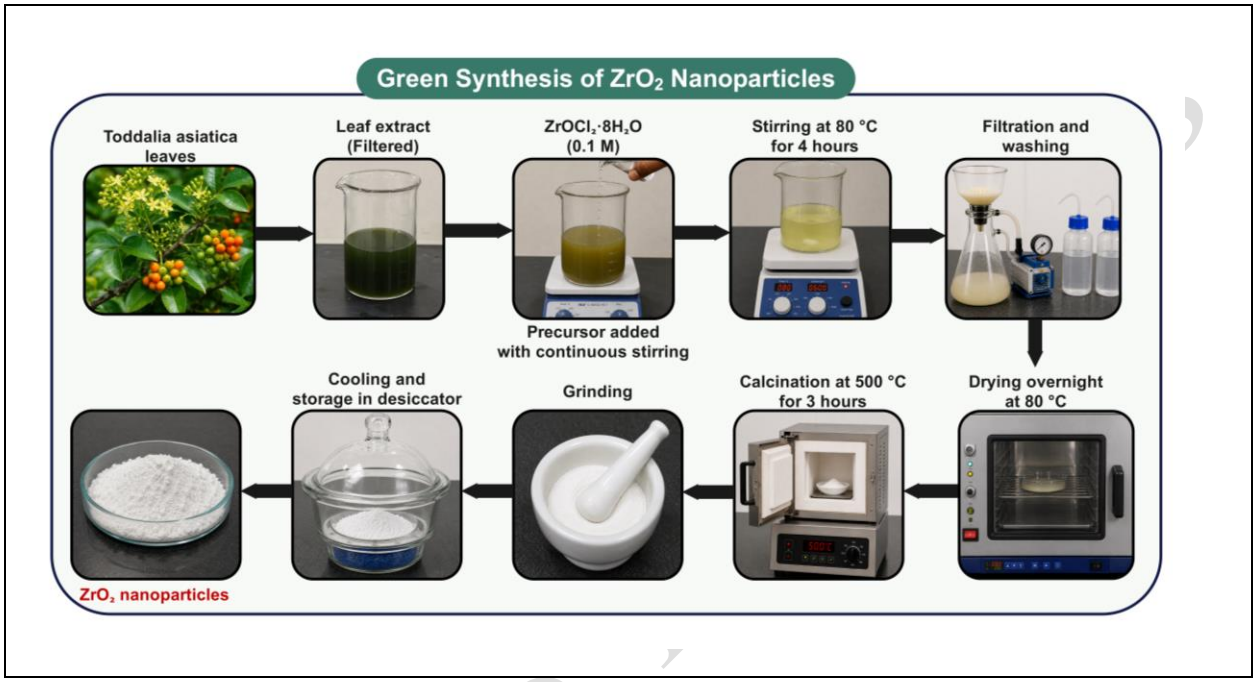


**Fig. 1: $ZrO_2$ nanoparticle synthesis**

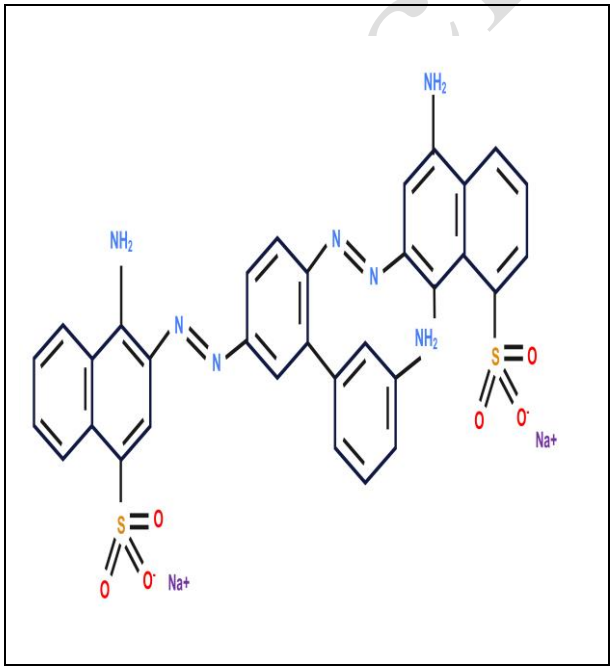


**Fig. 2: Congo red molecular structure**

**Table 1. Taguchi control factors and experimental levels**

| Factor | Level 1 | Level 2 | Level 3 | Unit |
|---|---|---|---|---|
| Initial CR concentration | 25 | 50 | 75 | mg $L^{-1}$ |
| Contact time | 30 | 60 | 90 | min |
| Temperature | 30 | 40 | 50 | °C |
| $ZrO_2$ nanoparticle dose | 0.25 | 0.50 | 0.75 | g $L^{-1}$ |

**Table 2. Output responses and optimization objectives**

| Response | Unit | Taguchi/MCDM Objective |
|---|---|---|
| Equilibrium adsorption capacity | mg $g^{-1}$ | Larger-the-better |
| Congo Red removal efficiency | % | Larger-the-better |

For a larger-the-better response, the signal-to-noise ratio was evaluated as:

$$S/N = -10 \log_{10}[(1/n)\,\Sigma_{i=1}^{n}\,(1/y_i^2)] \quad \ldots (5)$$

where n is the number of observations and $y_i$ is the observed response. A larger S/N ratio indicates better

response performance and reduced sensitivity to uncontrolled variation.

### 2.8 Analysis of Variance

ANOVA was applied separately to adsorption capacity and removal efficiency to quantify the statistical influence of each control factor. Factor significance was assessed at the 95% confidence level; therefore, p-values below 0.05 were statistically significant. F statistic and percentage contribution were calculated as:

$$F_j = MS_j / MS_e \quad \ldots (6)$$

$$\text{Contribution}_j\,(\%) = (SS_j / SS_t) \times 100 \quad \ldots (7)$$

where $MS_j$ and $SS_j$ are the mean square and sequential sum of squares of factor j, $MS_e$ is the error mean square, and $SS_t$ is the total sum of squares.

### 2.9 PSI Objective Weighting

The Preference Selection Index (PSI) method was used to determine objective weights for the two adsorption responses without assigning subjective expert preferences. The decision matrix $X = [x_{ij}]$ contained m = 27 alternatives and n = 2 criteria. Because both criteria were beneficial, normalization was performed using:

$$r_{ij} = x_{ij} / \max_i(x_{ij}) \quad \ldots (8)$$

The mean normalized performance of criterion j was calculated as:

$$\bar{r}_j = (1/m)\,\Sigma_{i=1}^{m}\, r_{ij} \quad \ldots (9)$$

To maintain scale stability for the 27-alternative matrix, normalized preference variation was calculated as the mean squared deviation:

$$PV_j = (1/m)\,\Sigma_{i=1}^{m}\,(r_{ij} - \bar{r}_j)^2 \quad \ldots (10)$$

$$\Phi_j = 1 - PV_j \quad \ldots (11)$$

$$w_j = \Phi_j / \Sigma_{j=1}^{n}\,\Phi_j \quad \ldots (12)$$

where $PV_j$ is the normalized preference variation, $\Phi_j$ is the deviation in preference value, and $w_j$ is the final PSI weight, with $\Sigma w_j = 1$.

### 2.10 PIV Alternative Ranking

The Proximity Indexed Value (PIV) method was subsequently applied to rank the 27 Taguchi alternatives using the PSI-derived weights. First, vector normalization was applied:

$$n_{ij} = x_{ij} / \sqrt{(\Sigma_{i=1}^{m}\, x_{ij}^2)} \quad \ldots (13)$$

The weighted normalized values were obtained as:

$$v_{ij} = w_j n_{ij} \quad \ldots (14)$$

For each benefit criterion, the positive ideal value was:

$$v_j^{+} = \max_i(v_{ij}) \quad \ldots (15)$$

The proximity difference and overall PIV score were calculated using:

$$d_{ij} = v_j^{+} - v_{ij} \quad \ldots (16)$$

$$PIV_i = \Sigma_{j=1}^{n}\, d_{ij} \quad \ldots (17)$$

The alternative with the smallest PIV score was assigned Rank 1 because it had the minimum aggregate distance from the positive ideal response.

### 2.11 Cascade-forward Artificial Neural Network

A cascade-forward artificial neural network (CFANN) was developed to model the nonlinear relationship between four adsorption variables and two output responses. The selected network contained four input neurons, eight hidden neurons, and two output neurons (4–8–2). In addition to the conventional layer-to-layer connection, the cascade-forward structure included direct connections from the input layer to subsequent layers. The hidden layer used a tangent-sigmoid activation function, while the output layer used a linear activation function.

$$f(n) = 2/[1 + \exp(-2n)] - 1 \quad \ldots (18)$$

Network weights and biases were adjusted using the Levenberg–Marquardt backpropagation algorithm. Input and output variables were scaled before training. The dataset was divided into training, validation, and testing subsets at a 70:15:15 ratio. The 27 experimental observations were divided into approximately 70% training, 15% validation, and 15% testing subsets, corresponding to 19 training, 4 validation, and 4 testing observations. Model performance was evaluated by root-mean-square error, coefficient of determination, mean absolute percentage error, and mean absolute error.

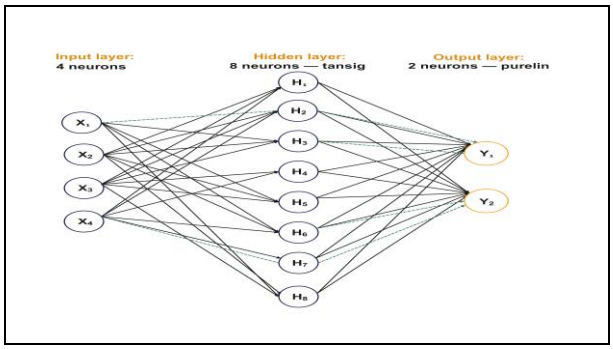


**Fig. 3: Cascade-forward artificial neural network architecture**

Article in Press

$$R^2 = 1 - [\Sigma_i(y_i - \hat{y}_i)^2 / \Sigma_i(y_i - \bar{y})^2] \quad \ldots (19)$$

$$RMSE = \sqrt{[(1/N)\Sigma_i(y_i - \hat{y}_i)^2]} \quad \ldots (20)$$

$$MAE = (1/N)\Sigma_i|y_i - \hat{y}_i| \quad \ldots (21)$$

$$MAPE\ (\%) = (100/N)\Sigma_i|(y_i - \hat{y}_i)/y_i| \quad \ldots (22)$$

### 2.12 Experimental Verification and CFANN-Based Optimization

The experimental condition ranked first by the PSI-PIV method was used to verify the predictive accuracy of the developed CFANN. For verification, the measured responses obtained at experimental Run 27 were compared directly with the corresponding CFANN-predicted values. At 75 mg $L^{-1}$ CR concentration, 90 min contact time, 40 °C, and 0.25 g $L^{-1}$ $ZrO_2$ dosage, the experimental removal efficiency and adsorption capacity were 63.56% and 33.05 mg $g^{-1}$, respectively, whereas CFANN predicted 63.6569% and 32.8634 mg $g^{-1}$. The corresponding prediction errors were 0.15% and 0.56%, respectively. Experimental responses were compared with the corresponding network predictions, and the prediction error was calculated as:

$$\text{Error}\ (\%) = \left|\frac{\text{Experimental} - \text{Predicted}}{\text{Experimental}}\right| \times 100 \ldots (23)$$

The validated CFANN was subsequently employed to predict the removal efficiency and adsorption capacity for all possible factor-level combinations. The predicted responses were normalized, weighted using the PSI method, and ranked through the PIV approach. Both responses were treated as beneficial criteria, and the combination with the lowest PIV index was selected as the CFANN-predicted multi-response optimum. The predicted optimum was then compared with the experimental PSI-PIV optimum to evaluate changes in factor settings and adsorption performance.

### 2.13 Adsorption Isotherm Analysis

Equilibrium data were fitted using the Freundlich, Temkin, and Langmuir isotherms to clarify the interaction between Congo Red and the $ZrO_2$ nanoparticle surface (Gaddala *et al.* 2025). These models were used to assess adsorption capacity, surface uniformity, adsorbate–adsorbent affinity and the energetic characteristics of the process.

Langmuir model with monolayer adsorption on a homogeneous surface with a finite number of equivalent sites. Its linear form is expressed as eqn(24):

$$\frac{C_e}{q_e} = \frac{1}{q_m K_L} + \frac{C_e}{q_m} \quad \ldots (24)$$

where , $q_e$ were the equilibrium adsorption capacity $(mgg^{-1}), C_e$ were the equilibrium CR concentration $(mgL^{-1})$ , $K_L$ were the Langmuir affinity constant $(Lmg^{-1})$ and $q_m$ were the theoretical monolayer capacity $(mgg^{-1})$. Adsorption favourability was evaluated using the separation factor:

$$R_L = \frac{1}{1+K_L C_0} \quad \ldots (25)$$

Values of $0 < R_L < 1, R_L > 1, R_L = 1$ and $R_L = 0$ represent favourable, linear, unfavourable, and irreversible adsorption.

Freundlich model describes adsorption on heterogeneous surfaces with sites of different energies and possible multilayer formation:

$$\log\ q_e = \log\ K_F + \frac{1}{n}\log\ C_e \quad \ldots (26)$$

where $K_F$ represents adsorption capacity and $n$ indicates adsorption intensity or surface heterogeneity. Temkin model considers adsorbate-adsorbent and assumes adsorption heat decreases linearly as surface coverage increases:

$$q_e = B\ln\ A_T + B\ln\ C_e \quad \ldots (27)$$

where $A_T$ were Temkin equilibrium binding constant ( $Lg^{-1}$ ) and $B$ is related to adsorption heat.

## 3. RESULTS AND DISCUSSION

### 3.1 Characterization of $ZrO_2$

#### 3.1.1 X-Ray Diffraction Analysis

XRD patterns of $ZrO_2$ nanoparticles before and after Congo Red adsorption were presented in Fig. 4. Main diffraction reflections were observed at approximately 2θ = 28.3°, 31.5°, 34.2°, 35.4°, 50.2°, 55.5°, and 60.0°, corresponding to (−111), (111), (002), (200), (220), (202), and (222) planes. These reflections indicate predominantly monoclinic $ZrO_2$, with the characteristic reflections near 2θ = 28.3° and 31.5° assigned to the (−111) and (111) planes, respectively, consistent with JCPDS No. 37-1484.

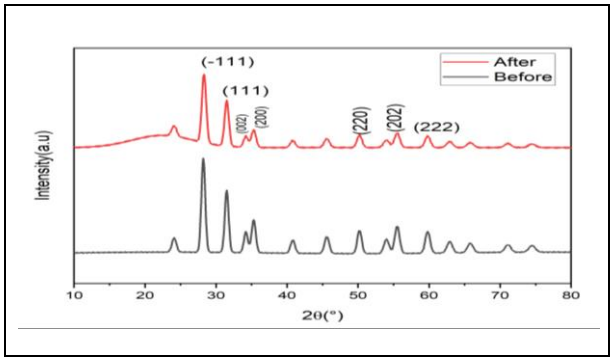


**Fig. 4: $ZrO_2$ before and after adsorption**

Article in Press

**Table 3. Crystallographic parameters of $ZrO_2$ nanoparticles**

| Crystal Parameter | Value |
|---|---|
| Crystal system | Monoclinic |
| α= γ | 90° |
| β | 99.2° |
| a | 0.515 nm |
| b | 0.521 nm |
| c | 0.531 nm |
| Dominant plane | (−111) |
| Dominant peak position | 28.3° |

The strong (−111) reflection suggests preferential crystallite development along this plane. No major displacement of the characteristic peaks was observed following CR adsorption, demonstrating that the $ZrO_2$ crystalline framework remained stable. The reduction in peak intensity and slight broadening after adsorption may be associated with CR coverage and interactions with surface-active sites.

Average crystallite size was determined using the Debye-Scherrer equation (28):

$$D = \frac{0.9\lambda}{\beta \cos\theta} \quad \ldots (28)$$

where $D$ represents crystallite size, $\lambda$ were X - ray wavelength, ,$\theta$ were Bragg angle and $\beta$ were full width. Broad diffraction peaks confirm the nanocrystalline character of the synthesized $ZrO_2$ material. In previous studies, XRD confirmed crystalline structure of $ZrO_2$ and showed that CQD incorporation reduced its crystallite size from 31 to 25 nm. This reduction indicated successful interaction and composite formation between CQD and $ZrO_2$ (Joshi *et al.* 2026).

### 3.1.2 FTIR Analysis

FTIR spectra of $ZrO_2$ nanoparticles recorded before and after Congo Red adsorption are shown in Fig. 5. Measurements were performed under ambient conditions over the wavenumber range of 4000–400 $cm^{-1}$.

Before adsorption, the broad band within 3425 $cm^{-1}$ was assigned to O–H stretching associated with physically adsorbed surface hydroxyl groups and adsorbed water. The absorption around 1630 $cm^{-1}$ originated from H–O–H bending vibrations. Bands located near 1394 and 1079 $cm^{-1}$ were attributed to residual oxygen-containing groups derived from the plant extract. The characteristic absorptions below approximately 745 and 525 $cm^{-1}$ corresponded to Zr–O and Zr–O–Zr bending and stretching modes, confirming formation of the zirconium oxide framework.

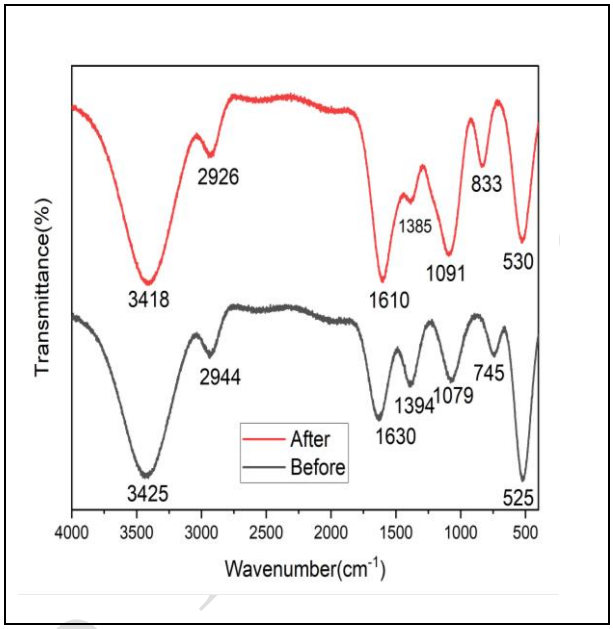


**Fig. 5: $ZrO_2$ spectra before and after adsorption**

Following CR adsorption, variations in band intensity and slight peak shifts were observed. The appearance or enhancement of bands around 1610 and 1385 $cm^{-1}$ was associated with aromatic and azo-group vibrations, whereas signals within 1091 and 833 $cm^{-1}$ were related to the sulfonate groups of CR. Changes in the hydroxyl and Zr–O regions suggest that surface –OH groups and zirconium-active sites participated in dye binding. These spectral variations support the adsorption of CR through hydrogen bonding, electrostatic attraction, and surface complexation while indicating that the fundamental $ZrO_2$ structure was retained. In prior studies, FTIR analysis of *Toddalia asiatica* root extracts revealed characteristic O–H, C=O, and aromatic functional groups associated with its diverse phytoconstituents. These functional groups confirmed the structural diversity and phytochemical richness of the plant extract (Ramalakshmi *et al.* 2026).

### 3.1.3 SEM-EDX Analysis

SEM–EDX analysis was employed to investigate surface morphology and elemental composition of $ZrO_2$ nanoparticles before and after Congo Red adsorption. As shown in Fig. 6(a,b), synthesized nanoparticles showed irregular, aggregated particles with a rough and heterogeneous surface. Interparticle spaces, surface cavities, and porous regions were observed throughout the agglomerated structure, potentially providing accessible sites for dye adsorption.

Article in

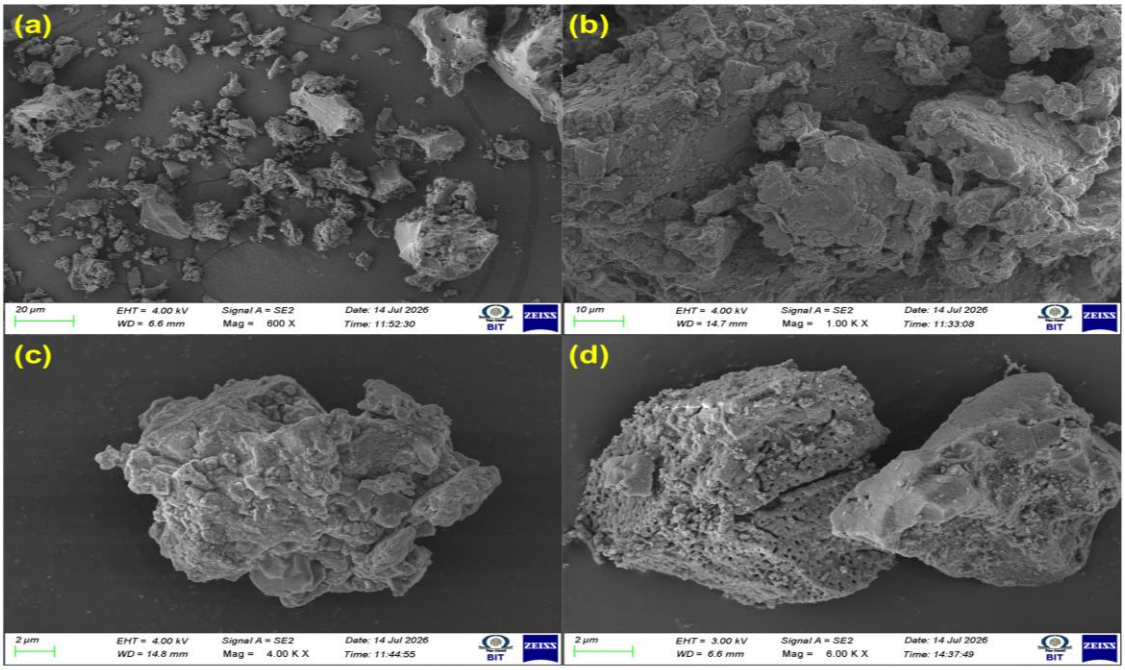


**Fig. 6: SEM–EDX of CR-loaded $ZrO_2$**

Following CR adsorption, Fig. 6(c,d) showed aggregated particles with comparatively compact and rough surface structures**.** Partial surface coverage and reduced visibility of some cavities may be associated with accumulation of CR molecules within available surface sites and interparticle spaces. However, because the micrographs were recorded at different magnifications, these morphological differences should be interpreted cautiously. The original agglomerated framework remained distinguishable, indicating that adsorption did not cause substantial structural degradation.

Before adsorption, the EDX spectrum was dominated by zirconium and oxygen, confirming the formation of $ZrO_2$. A minor carbon signal may originate from residual phytochemicals or the carbon adhesive used during sample preparation. After adsorption, increased carbon and the appearance of sulfur and sodium signals were associated with the aromatic and sulfonate components of CR. If supported by elemental mapping, the distribution of these elements across the $ZrO_2$ surface confirms successful dye uptake. The combined SEM and EDX observations therefore demonstrate surface coverage and elemental changes resulting from interaction between CR molecules and active $ZrO_2$ adsorption sites. As reported in prior studies, SEM analysis revealed the surface morphology and distribution of vanadium species over the mixed-phase $ZrO_2$ nanoparticles. EDX confirmed the presence of Zr, O, and V elements, verifying successful incorporation of vanadium into the $ZrO_2$ photocatalyst (Tahir *et al*. 2026).

### 3.1.4 X-ray Fluorescence Analysis

XRF analysis was used to determine the oxide composition of the $ZrO_2$ nanomaterial before and after Congo Red adsorption. Zirconium dioxide was the predominant component before adsorption, while other detected oxides occurred only in minor proportions.

**Table 4. XRF composition of $ZrO_2$ nanoparticles**

| Sample | $ZrO_2$ (%) | $HfO_2$ (%) | $SiO_2$ (%) | $Fe_2O_3$ (%) | $Na_2O$ (%) | $SO_3$ (%) |
|---|---|---|---|---|---|---|
| Before adsorption | 96.20 | 1.70 | 1.00 | 0.70 | 0.30 | 0.10 |
| After CR adsorption | 87.00 | 1.50 | 0.90 | 0.60 | 2.80 | 7.20 |

After adsorption, the relative $ZrO_2$ percentage decreased because the XRF results were normalized in the presence of dye-derived components. An increase in $SO_3$ and $Na_2O$ was associated with the sulfonate and sodium groups of CR. These compositional variations support the attachment of CR molecules to the $ZrO_2$ surface.

### 3.1.5 TGA–DTA Analysis

The TGA–DTG profile showed a progressive decrease in residual mass from approximately 90% at the

beginning of heating to about 78% at 100 °C, 64% at 300 °C, 47% at 600 °C, and approximately 14% at 900 °C. The DTG profile exhibited thermal events near 75 and 300 °C, followed by pronounced high-temperature mass loss approaching 900 °C. Therefore, substantial mass loss continued above 600 °C, and the present curve does not indicate a stable mass plateau in this region.

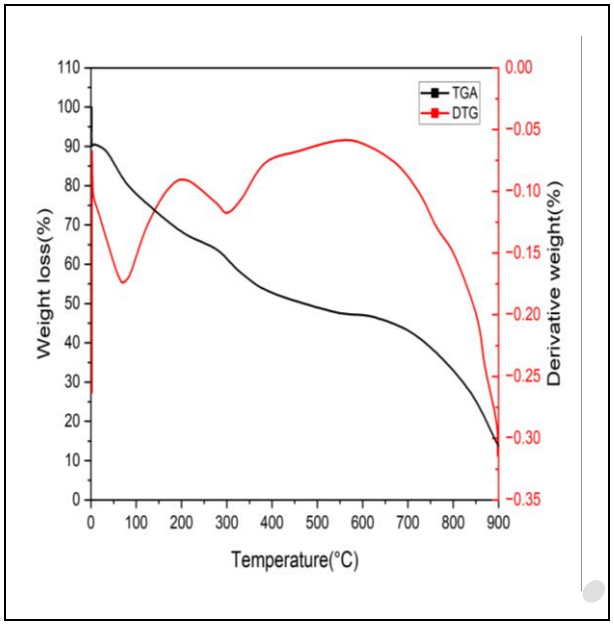


**Fig. 7: Thermal behaviour of $ZrO_2$**

Above approximately 600 °C, only a minor mass change was observed, indicating the formation of a thermally stable $ZrO_2$ phase. The corresponding DTA curves, particularly near 75, 300, and 900 °C represented the dehydration and decomposition of the remaining surface-bound species. Previous studies have demonstrated that the TGA confirmed the thermal stability of the g-$C_3N_4$–$ZrO_2$ nanocomposite and identified weight-loss stages associated with moisture removal and decomposition of surface-bound components. The results confirmed that incorporating $ZrO_2$ improved the composite's structural stability under elevated temperatures (Shinde *et al.* 2026).

## 3.2 Optimization

### 3.2.1 Taguchi Effects on Congo Red Removal Efficiency

**Table 5. Taguchi response statistics for congo red removal efficiency**

| Statistic | Initial Concentration | Contact Time | Temperature | Dosage |
|---|---|---|---|---|
| Mean—Level 1 | 73.68 | 67.56 | 67.69 | 62.58 |
| Mean—Level 2 | 70.84 | 71.15 | 71.00 | 71.07 |
| Mean—Level 3 | 68.76 | 74.57 | 74.59 | 79.63 |
| Mean delta (rank) | 4.92 (4) | 7.01 (2) | 6.90 (3) | 17.06 (1) |
| S/N—Level 1 | 37.30 | 36.51 | 36.53 | 35.89 |
| S/N—Level 2 | 36.95 | 37.03 | 37.01 | 37.03 |
| S/N—Level 3 | 36.68 | 37.39 | 37.39 | 38.00 |
| S/N delta (rank) | 0.61 (4) | 0.88 (2) | 0.86 (3) | 2.11 (1) |

The mean removal efficiency decreased from 73.68% to 68.76% as initial CR concentration raised from 25 to 75 mg $L^{-1}$. This behaviour indicates that a larger number of CR molecules competed for a finite population of accessible $ZrO_2$ surface sites. In contrast, longer contact time enhanced removal from 67.56% at 30 min to 74.57% at 90 min, consistent with continued dye transfer and progressive occupation of available adsorption sites.

Raising temperature from 30 to 50 °C increased the mean removal from 67.69% to 74.59%, suggesting that mass transfer and the accessibility of active sites improved within the investigated range. Dosage exerted the strongest effect: the mean removal rose from 62.58% at 0.25 g $L^{-1}$ to 79.63% at 0.75 g $L^{-1}$ because greater solid loading supplied more adsorption sites. Both the mean and S/N analyses ranked dosage first and selected $A_1B_3C_3D_3$ as the removal-efficiency optimum.

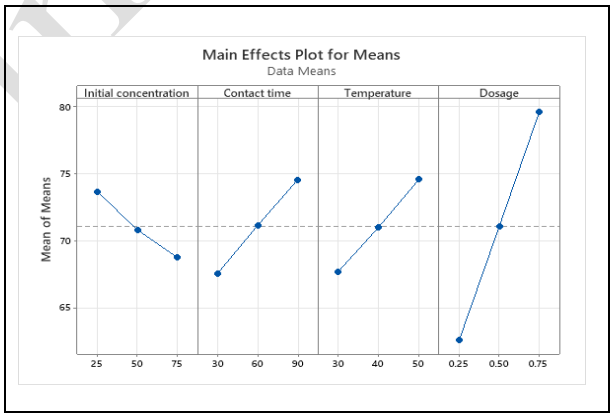


**Fig. 8: Main-effect plot of factor means for congo red removal efficiency**

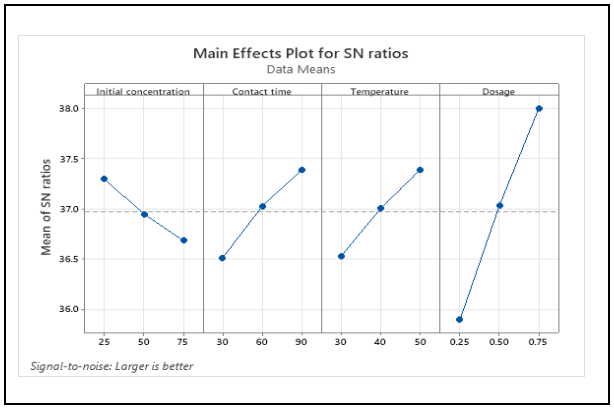


**Fig. 9: Main-effect plot of larger-the-better S/N ratios for Congo red removal efficiency**

Article in Press

### 3.2.2 Taguchi effects on adsorption capacity

**Table 6. Taguchi response statistics for equilibrium adsorption capacity**

| Statistic | Initial Concentration | Contact Time | Temperature | Dosage |
|---|---|---|---|---|
| Mean—Level 1 | 17.89 | 21.03 | 21.46 | 26.98 |
| Mean—Level 2 | 22.54 | 22.51 | 22.53 | 22.45 |
| Mean—Level 3 | 27.03 | 23.92 | 23.48 | 18.03 |
| Mean delta (rank) | 9.14 (1) | 2.90 (3) | 2.02 (4) | 8.95 (2) |
| S/N—Level 1 | 24.83 | 26.17 | 26.39 | 28.51 |
| S/N—Level 2 | 26.92 | 26.74 | 26.70 | 26.90 |
| S/N—Level 3 | 28.55 | 27.39 | 27.21 | 24.88 |
| S/N delta (rank) | 3.72 (1) | 1.21 (3) | 0.82 (4) | 3.63 (2) |

Adsorption capacity displayed the opposite concentration and dosage trends. Increasing the initial CR concentration raised mean $q_e$ from 17.89 to 27.03 mg $g^{-1}$ because the larger concentration gradient increased the driving force for solute transfer and the amount of dye available per unit adsorbent. Conversely, increasing dosage reduced $q_e$ from 26.98 to 18.03 mg $g^{-1}$. Contact time and temperature produced smaller positive effects on capacity. The factor order from both the means and S/N ratios was initial concentration > dosage > contact time > temperature. The single-response capacity optimum was $A_3B_3C_3D_1$.

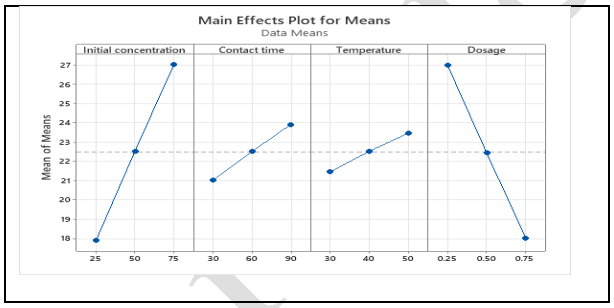


**Fig. 10: Main-effect plot of factor means for equilibrium adsorption capacity**

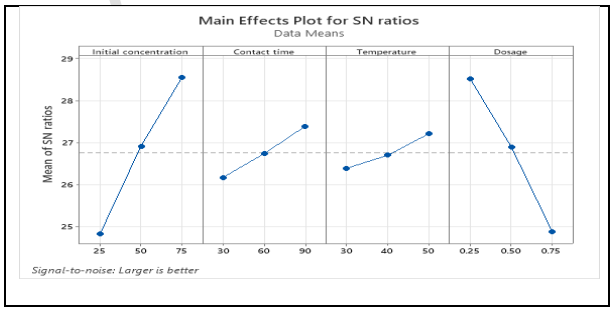


**Fig. 11: Main-effect plot of larger-the-better S/N ratios for equilibrium adsorption capacity**

### 3.2.3 ANOVA

**Table 7. ANOVA results for congo red removal efficiency**

| Source | DF | Contribution (%) | F-value | p-value |
|---|---|---|---|---|
| Initial concentration | 2 | 5.92 | 635.14 | <0.001 |
| Contact time | 2 | 11.91 | 1276.73 | <0.001 |
| Temperature | 2 | 11.56 | 1238.92 | <0.001 |
| Dosage | 2 | 70.53 | 7560.47 | <0.001 |
| Residual | 18 | 0.08 | — | — |

**Table 8. ANOVA results for equilibrium adsorption capacity**

| Source | DF | Contribution (%) | F-value | p-value |
|---|---|---|---|---|
| Initial concentration | 2 | 47.36 | 2513.50 | <0.001 |
| Contact time | 2 | 4.76 | 252.43 | <0.001 |
| Temperature | 2 | 2.32 | 122.87 | <0.001 |
| Dosage | 2 | 45.40 | 2409.45 | <0.001 |
| Residual | 18 | 0.17 | — | — |

Dosage accounted for 70.53% of the variability in removal efficiency, whereas contact time and temperature contributed 11.91% and 11.56%, respectively. Initial concentration contributed only 5.92%. The removal model achieved $R^2$ = 99.92%, adjusted $R^2$ = 99.88% and predicted $R^2$ = 99.81%. For adsorption capacity, initial concentration and dosage were dominant, contributing 47.36% and 45.40%, respectively. Contact time and temperature accounted for 4.76% and 2.32%. The capacity model produced $R^2$ = 99.83%, adjusted $R^2$ = 99.76% and predicted $R^2$ = 99.62%. All factor p-values were below 0.001. Earlier studies, ANOVA by Tukey's post-hoc test with significant differences between the antibacterial activities of individual and combined extracts of *Toddalia asiatica, Aloe secundiflora, Senna didymobotrya,* and *Camellia sinensis* ($p < 0.05$) (Odongo *et al.* 2023).

### 3.2.4 PSI–PIV multi-response optimization of the experimental runs

**Table 9. PSI weights used for multi-response ranking**

| Criterion | PSI Weight | Criterion Direction |
|---|---|---|
| Removal efficiency | 0.504653 | Beneficial |
| Adsorption capacity | 0.495347 | Beneficial |
| Total | 1.000000 | — |

The PSI method assigned nearly equal weights to removal efficiency (0.504653) and adsorption capacity (0.495347), indicating their balanced importance. Both beneficial criteria were subsequently integrated into the PIV method to identify the best compromise adsorption condition.

**Table 10. Ten highest-ranked experimental PSI–PIV alternatives**

| Rank | Run | A | B | C | D | Removal (%) | $q_e$ (mg $g^{-1}$) | PIV |
|---|---|---|---|---|---|---|---|---|
| 1 | 27 | 75 | 90 | 40 | 0.25 | 63.56 | 33.05 | 0.034791 |
| 2 | 15 | 75 | 60 | 50 | 0.25 | 63.52 | 32.46 | 0.037277 |
| 3 | 9 | 75 | 90 | 50 | 0.75 | 84.56 | 24.87 | 0.040006 |
| 4 | 26 | 50 | 90 | 40 | 0.25 | 65.69 | 28.52 | 0.050569 |
| 5 | 14 | 50 | 60 | 50 | 0.25 | 66.01 | 28.17 | 0.051577 |
| 6 | 18 | 75 | 90 | 30 | 0.50 | 68.74 | 27.16 | 0.052035 |
| 7 | 21 | 75 | 30 | 50 | 0.50 | 69.08 | 26.95 | 0.052439 |
| 8 | 6 | 75 | 60 | 40 | 0.50 | 68.60 | 26.67 | 0.054245 |
| 9 | 8 | 50 | 90 | 50 | 0.75 | 86.09 | 20.09 | 0.057629 |

The PSI–PIV analysis ranked Run 27 as the best experimental alternative, recording the lowest PIV index of 0.034791 with 63.56% removal efficiency and an adsorption capacity of 33.05 mg $g^{-1}$. Thus, $A_3B_3C_2D_1$ were identified as optimal compromise condition for both responses.

### 3.2.5 CFANN Prediction Performance

**Table 11. CFANN performance metrics**

| Subset | Response | $R^2$ | R | RMSE | MAE | MAPE (%) |
|---|---|---|---|---|---|---|
| Training | Removal | 0.99795 | 0.99898 | 0.34643 | 0.23165 | 0.32644 |
| Training | Capacity | 0.99885 | 0.99964 | 0.18670 | 0.13836 | 0.69557 |
| Validation | Removal | 0.99722 | 0.99969 | 0.68142 | 0.59825 | 0.89026 |
| Validation | Capacity | 0.99835 | 0.99947 | 0.21279 | 0.18547 | 0.91468 |
| Testing | Removal | 0.97877 | 0.99751 | 0.62615 | 0.52037 | 0.75870 |
| Testing | Capacity | 0.97012 | 0.98957 | 0.77772 | 0.66525 | 2.93830 |
| Overall | Removal | 0.99693 | 0.99866 | 0.45971 | 0.32873 | 0.47400 |
| Overall | Capacity | 0.99589 | 0.99813 | 0.34763 | 0.22340 | 1.06030 |

The 4-8-2 CFANN demonstrated strong predictive performance for both responses. The overall $R^2$ values were 0.99693 for removal efficiency and 0.99589 for adsorption capacity, with corresponding MAPE values of 0.474% and 1.060%. Test $R^2$ values of 0.97877 and 0.97012 further confirmed the satisfactory generalization of the developed model. Similarly, in the prior studies, the $ZrO_2$-pumice/$H_2O_2$-catalysed ozonation system effectively removed Rhodamine B through a hydroxyl-radical-mediated mechanism, with CCD-RSM and ANN producing $R^2$ values of 0.9998 and 0.9948, respectively. The hybrid process enhanced removal by 51.9%, achieved 64.4% TOC removal, improved wastewater biodegradability, and maintained reasonable catalyst performance over five cycles (Shokoohi *et al.* 2021).

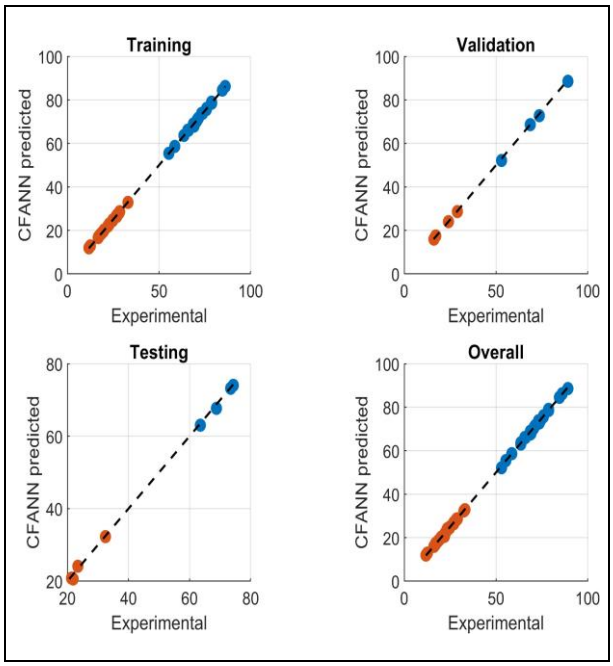


**Fig. 12: Experimental versus CFANN-predicted responses for the training, validation, testing, and overall datasets**

Article in Press

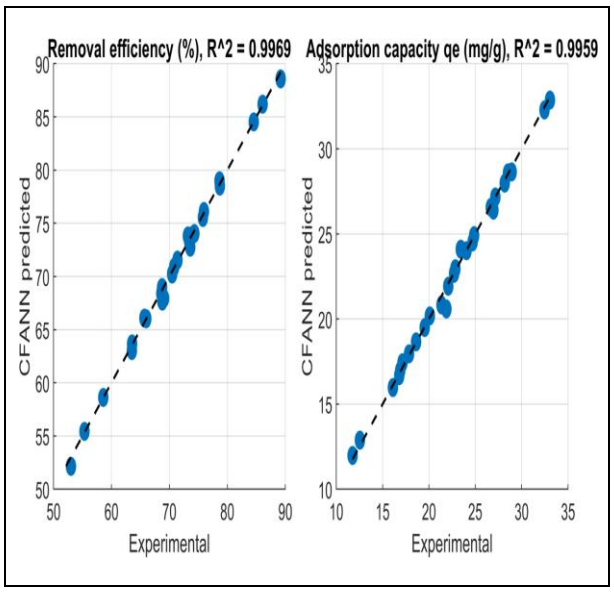


**Fig. 13: Overall experimental-versus-predicted agreement for (a) removal efficiency and (b) adsorption capacity**

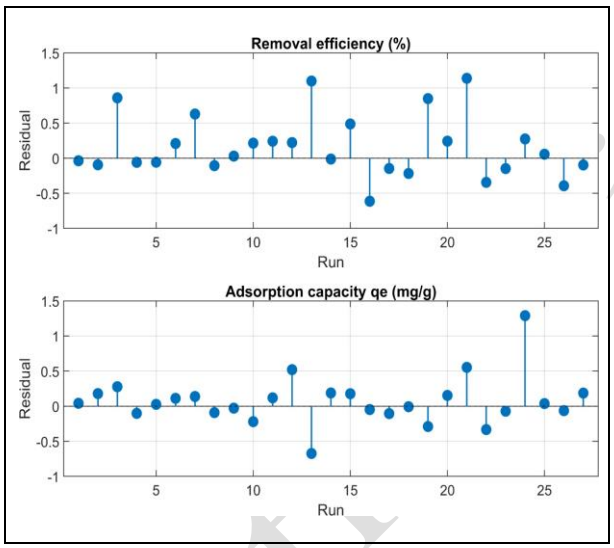


**Fig. 14: CFANN prediction residuals for removal efficiency and adsorption capacity**

The points in Figure 13 cluster closely around the equality line. Residuals in Figure 14 fluctuate around zero without a clear monotonic pattern. The largest listed capacity percentage error occurred at Run 24 (5.89%), but the overall capacity MAPE remained low.

## 3.3 Experimental Verification and CFANN-Predicted Optimum

The CFANN predictions for experimental Run 27 closely agreed with the measured responses, with errors of only 0.15% for removal efficiency and 0.56% for adsorption capacity (Table 12). This close agreement confirms the predictive accuracy of the developed CFANN at the experimental PSI–PIV optimum.

**Table 12. CFANN verification at experimental Run 27**

| Response | Experimental | CFANN Predicted | Error (%) |
|---|---|---|---|
| Removal efficiency (%) | 63.56 | 63.6569 | 0.15 |
| Adsorption capacity ( $mgg^{-1}$ ) | 33.05 | 32.8634 | 0.56 |

CFANN-PSI-PIV evaluation of all factor combinations identified $A_3B_3C_3D_1$ as the predicted optimum. This condition corresponded to $75 mgL^{-1}$ initial concentration, 90 min contact time, 50 °C and $0.25\ g\ L^{-1}$ dosage, yielding predicted removal efficiency and adsorption capacity of 67.2169% and $33.9606 mgg^{-1}$, respectively. Compared with the experimental optimum, the predicted condition retained the same concentration, contact time, and dosage but increased the temperature from 40 to 50°C (Table 13).

**Table 13. Comparison of the experimental and CFANN-predicted optimum conditions**

| Parameter | Experimental PSI-PIV Optimum | CFANN-Predicted Optimum |
|---|---|---|
| Condition | $A_3B_3C_2D_1$ | $A_3B_3C_3D_1$ |
| Initial concentration ($mgL^{-1}$) | 75 | 75 |
| Contact time (min) | 90 | 90 |
| Temperature ( °C) | 40 | 50 |
| Dosage ( $gL^{-1}$ ) | 0.25 | 0.25 |
| Removal efficiency (%) | 63.56 | 67.2169 |
| Adsorption capacity ( $mgg^{-1}$ ) | 33.05 | 33.9606 |
| PIV index | 0.034791 | 0.016968 |

The condition of 75 mg $L^{-1}$ CR, 90 min, 50 °C, and 0.25 g $L^{-1}$ $ZrO_2$ represents the CFANN–PSI–PIV model-predicted optimum, with a predicted removal efficiency of 67.2169% and an adsorption capacity of 33.9606 mg $g^{-1}$. This condition was not independently validated experimentally and therefore requires confirmatory experimentation. The lower predicted PIV index indicates an improved balance between removal efficiency and adsorption capacity.

## 3.4 Adsorption Equilibrium Study

Equilibrium adsorption of Congo Red onto $ZrO_2$ nanoparticles was evaluated using Langmuir, Freundlich and Temkin models. Corresponding isotherm plots are presented in Fig. 15, while calculated parameters were summarized in Table 14. The Langmuir model gave $q_m$ = 286.64 mg $g^{-1}$, $K_l$ = 0.1108 L $mg^{-1}$, and $R^2$ = 0.99997. The Freundlich model produced K_F = 48.46, 1/n = 0.4167 and $R^2$ = 0.93139, whereas the Temkin model yielded A_T = 1.303 L $g^{-1}$, B = 57.45 J $mol^{-1}$ and $R^2$ = 0.99227.

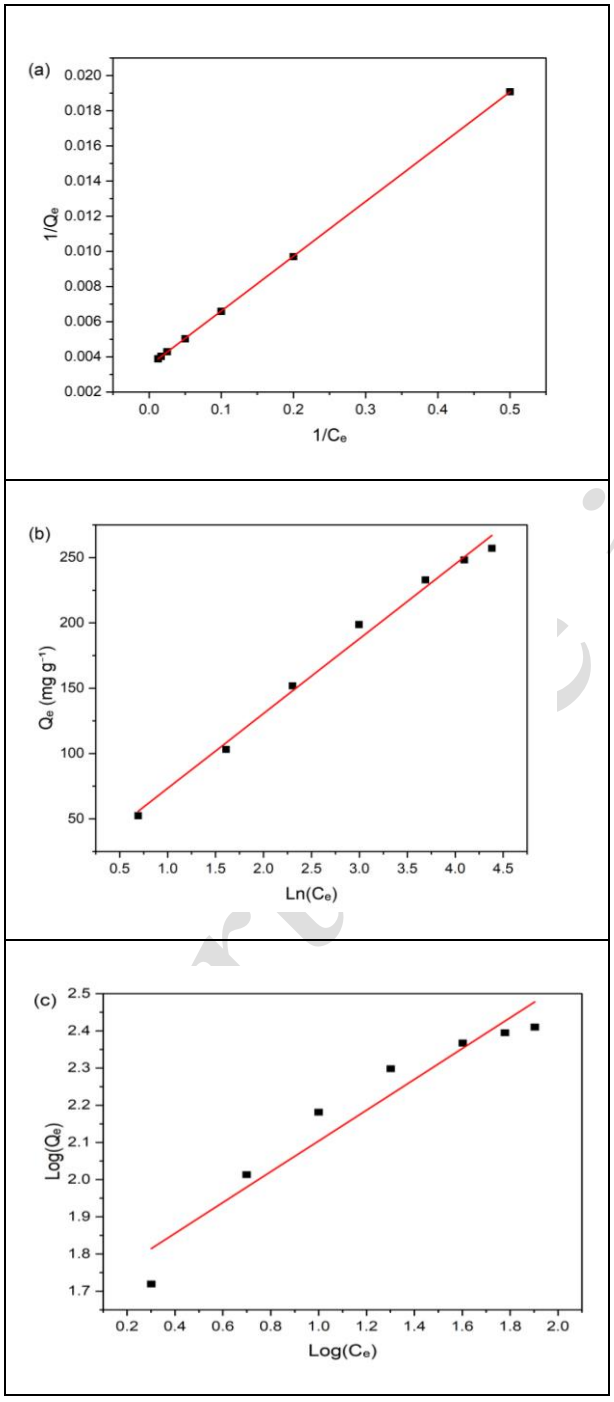


**Fig. 15: CR adsorption isotherm models**

**Table 14. Isotherm parameters for CR adsorption**

| Isotherm | Parameter | Value |
|---|---|---|
| Langmuir | ($q_m$) (mg $g^{-1}$) | 286.64 |
| | ($K_L$) (L $mg^{-1}$) | 0.1108 |
| | ($R^2$) | 0.99997 |
| Freundlich | (1/n) | 0.4167 |
| | ($K_F$) | 48.46 |
| | ($R^2$) | 0.93139 |
| Temkin | (B) (J $mol^{-1}$) | 57.45 |
| | ($A_T$) (L $g^{-1}$) | 1.303 |
| | ($R^2$) | 0.99227 |

Among the investigated models, Langmuir produced the highest $R^2$ value of 0.99997, compared with 0.93139 for Freundlich and 0.99227 for Temkin. The Langmuir maximum capacity was 286.64 mg $g^{-1}$, while the affinity constant was $0.1108 Lmg^{-1}$. These results indicate favourable CR uptake and predominantly monolayer adsorption on relatively uniform $ZrO_2$ surface sites. The Freundlich value of $1/n = 0.4167$ also confirms favourable adsorption because it lies between zero and one. However, its lower $R^2$ demonstrates that surface heterogeneity was less dominant than the monolayer mechanism. In prior research, the Langmuir isotherm provided the best fit for Congo Red adsorption onto the $Ag_2O$–$Al_2O_3$–$ZrO_2$/rGO composite, showing monolayer adsorption on active sites. The composite achieved a maximum adsorption capacity of 333.32 mg $g^{-1}$ (Sharma *et al.* 2021).

## 3.5 Cyclic Reuse $ZrO_2$

The regeneration performance of $ZrO_2$ nanoparticles was evaluated for eight successive adsorption–desorption cycles. After each adsorption cycle, the nanoparticles were recovered, rinsed with distilled water, and dispersed in ethanol under stirring to desorb retained Congo Red. The regenerated adsorbent was then filtered, washed, and dried before reuse in the subsequent cycle.

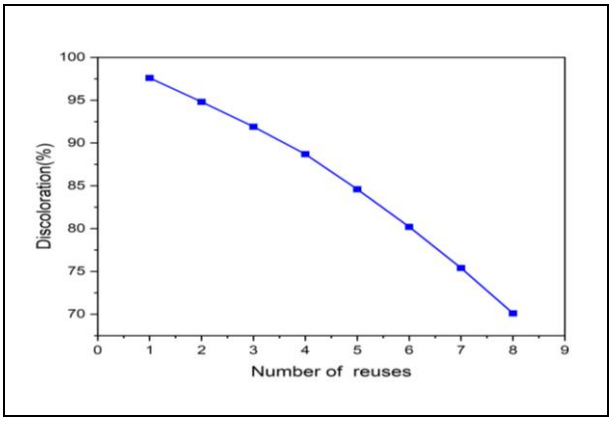


**Fig. 16 $ZrO_2$ Regeneration cycle performance**

The values in Fig. 16 represent relative adsorption-performance retention after regeneration rather than absolute Congo Red removal efficiency. Relative performance decreased from approximately 97.5% after the first regeneration to 70.0% after the eighth cycle. Although adsorption performance gradually decreased, the material maintained considerable activity after repeated use. The reduction may be associated with incomplete dye desorption, progressive obstruction of active sites, and minor adsorbent loss during recovery. Overall, the results demonstrate the regeneration stability and reuse potential of $ZrO_2$ nanoparticles for CR-contaminated water treatment.

## 4. CONCLUSIONS

Green synthesis of predominantly monoclinic $ZrO_2$ nanoparticles was achieved using zirconyl chloride octahydrate and *Toddalia asiatica* leaf extract, with an estimated crystallite size of 12.22 nm. ANOVA identified $ZrO_2$ dosage as the dominant factor governing Congo Red removal with a 70.53% contribution, whereas initial concentration and dosage contributed 47.36% and 45.40%, respectively, to adsorption capacity. PSI–PIV identified Run 27 at 75 mg $L^{-1}$, 90 min, 40 °C, and 0.25 g $L^{-1}$ as the best experimental compromise. The 4–8–2 CFANN achieved overall $R^2$ values of 0.99693 and 0.99589 for removal efficiency and adsorption capacity, respectively. CFANN–PSI–PIV predicted an optimum at 75 mg $L^{-1}$, 90 min, 50 °C, and 0.25 g $L^{-1}$, with 67.2169% predicted removal. These findings demonstrate laboratory-scale potential for Congo Red adsorption; however, validation using real wastewater, competing ions, continuous-flow operation, and extended regeneration is required before industrial application.

## FUNDING

This research received no specific grant from any funding agency in the public, commercial, or not-for-profit sectors.

## CONFLICTS OF INTEREST

The authors declare that there is no conflict of interest.

## COPYRIGHT

This article is an open-access article distributed under the terms and conditions of the Creative Commons Attribution (CC BY) license (http://creativecommons.org/licenses/by/4.0/).

## REFERENCES

Amale, A. B., Satishkumar, P., Bhagat, P. R., Motghare, M. S. and Krishnaraj, C., Green Synthesis of ZnO Nanoparticles Using Azadirachta indica Leaf Extract for Rapid Catalytic Degradation of Organic Pollutants, *J. Environ. Nanotechnol.*, 15(2), 151–161 (2026). https://doi.org/10.13074/jent.2026.06.2612082

Das, R. S., Kumar, A., Wankhade, A. V. and Peshwe, D. R., $ZrO_2$@chitosan composite for simultaneous photodegradation of three emerging contaminants and antibacterial application, *Carbohydrate Polym.*, 278, 118940 (2022). https://doi.org/10.1016/j.carbpol.2021.118940

Gaddala, B., Devi, K. V, Balakrishnan, V., Sundramurthy, V. P., Hariprabhu, M., Mayakannan, S., Kadaikunnan, S. and Khaled, J. M., Evaluation of detoxification performance of Pithecellobium dulce seed pod powder upon acid treatment: removal of reactive red 195-A dye and kinetic analysis, *Zeitschrift für Physikalische Chemie*, 239(6), 885–910 (2025). https://doi.org/10.1515/zpch-2024-0879

Halder, P., Mondal, I., Mukherjee, A., Biswas, S., Sau, S., Mitra, S., Paul, B. K., Mondal, D., Chattopadhyay, B. and Das, S., $Te_4$+ and $Er_3$+ doped $ZrO_2$ nanoparticles with enhanced photocatalytic, antibacterial activity and dielectric properties: A next generation of multifunctional material, *J. Environ. Manage.*, 359, 120985 (2024). https://doi.org/10.1016/j.jenvman.2024.120985

Joshi, A. J., Bhoi, B., Singh, D. K. and Chandra, V., Solar responsive CQD/$ZrO_2$ nanocomposites for rapid degradation of Reactive Red-120, *Mater. Chem. Phys.*, 360, 132565 (2026). https://doi.org/10.1016/j.matchemphys.2026.132565

Kathirvel, A., Srinivasan, R., Harini, S., Ranjith, N., Kumar, G. S., Lalithambigai, K., Atchudan, R., Habila, M. A., Aljuwayid, A. M. and Yun, H. K., Eco-Friendly Synthesis of Zirconium Dioxide Nanoparticles from *Toddalia asiatica*: Applications in Dye Degradation, Antioxidant and Antibacterial Activity, *Nanomater.*, 15(2), 84 (2025). https://doi.org/10.3390/nano15020084

Li, S., Zhang, H., Xiang, B., Chen, G., Huang, J., Mo, Y., Zhong, C., Xiang, D. and Wu, J., Novel Ag-m-t-$ZrO_2$ nanocomposite photocatalyst derived from $NH_2$-UiO-66 with enhanced degradation of dye wastewater under visible light and antibacterial performance, *Colloids Surf. A: Physicochem. Eng. Aspects*, 747, 140890 (2026). https://doi.org/10.1016/j.colsurfa.2026.140890

Mungle, N. P., Deshmukh, M. S., Satishkumar, P., Talodhikar, V., Kakade, N. T., Clement, M. and Gounder, K. N., Green Synthesis of $MnFe_2O_4$ Spinel Nanoparticles Using Camellia sinensis Extract: Optical Bandgap Engineering and Sunlight-driven Photocatalytic Wastewater Remediation, *J. Environ.*

Article in Press

*Nanotechnol.*, 15(2), 73–89 (2026). https://doi.org/10.13074/jent.2026.06.2612103

Nadesan, A., Subramanian, P., Amaladoss, N., Sivaraman, R. M., Sudhakar, S. and Taras, T., Rubidium-doped zirconia nanoparticles: Green synthesis, structural characterization, and enhanced photocatalytic degradation of malachite green dye, *Next Nanotechnol.*, 10, 100617 (2026). https://doi.org/10.1016/j.nxnano.2026.100617

Odongo, E. A., Mutai, P. C., Amugune, B. K., Mungai, N. N., Akinyi, M. O. and Kimondo, J., Evaluation of the antibacterial activity of selected Kenyan medicinal plant extract combinations against clinically important bacteria, *BMC Complement. Med. Therapies*, 23(1), 100 (2023). https://doi.org/10.1186/s12906-023-03939-4

Paul, S. R., Das, T., Debnath, A., Misra, T. K. and Chellam, P. V., Enhanced sequestration of malachite green dye from aqueous medium using zirconium oxide modified biochar from aegle marmelos: mechanism, reusability, and economic evaluation, *J. Ind. Chem. Soc.*, 103(9), 102895 (2026). https://doi.org/10.1016/j.jics.2026.102895

Qi, W., Yang, Y., Du, J., Yang, J., Guo, L. and Zhao, L., Highly photocatalytic electrospun Zr/Ag Co-doped titanium dioxide nanofibers for degradation of dye, *J. Colloid Interf. Sci.*, 603, 594–603 (2021). https://doi.org/10.1016/j.jcis.2021.06.109

Rajeswaran, P., Balaramesh, P., Vijayakumar, B., Muralidharan, V. P., Subha, V. and Selvarani, V., Ficus carica Fruit Extract Mediated Synthesis of $ZrO_2$ Nanoparticles for Enhanced Photocatalytic Degradation and Environmental Remediation, *Waste Biomass Valoriz.*, 17(1), 85–99 (2026). https://doi.org/10.1007/s12649-025-03097-3

Rajput, K., Vazquez, C. J., Jorge, S. A. B., Dev, S. M. and Crick, C. R., Recyclable and eco-compatible polymer composite nanofibers for broad-spectrum dye remediation, *RSC Appl. Polym.*, 4(2), 725–735 (2026). https://doi.org/10.1039/d5lp00307e

Ramalakshmi, P., Annapoorani, P., Rekha, A., Vijayan, R. and Arjun, P. Identification of Compounds Using *Toddalia asiatica* Analytical Methods with Molecular Docking Insights into PI3KA And EGFR, *Rasayan J. Chem.*, 19(1), 294–308 (2026). https://doi.org/10.31788/RJC.2026.1919562

Rana, R., Ahmad, W., Hawwal, M. F., Ansari, I. A., Kumar, S. and Ahmed, S., Nifedipine and metronidazole photodegradation using sustainable Raphanus sativus leaf extract mediated zirconia nanoparticles: A novel green solution for pharmaceutical waste treatment, *Environ. Progress Sustainable Energy*, 70523 (2026). https://doi.org/10.1002/ep.70523

Rao, D. P., Krishnasamy, V. D., Selvaraju, M., Sundramurthy, V. P., Kandavalli, S. R., Chitra, M. S., Sivasamy, N. and Thirumoorthy, P., Adsorptive removal of cadmium from electroplating wastewater using hybrid composite of thiol-grafted seed gum of Tamarindus indica and Teff hay biocarbon, *Zeitschrift für Physikalische Chemie,* 239(5), 633–654 (2025). https://doi.org/10.1515/zpch-2024-0715

Senthilkumar, N., Karthikeyan, K., Dhamodaran, M., Vijayan, V., Jeevitha, T. U., Eswaramoorthy, N., Chellamuthu, K. and Sasikumar, A., Electrospun PVA/$ZrO_2$, PVA/CuO, and PVA/α-$Fe_2O_3$ nanocomposites: A comparative study on photocatalytic activity, *Vacuum*, 252, 115417 (2026). https://doi.org/10.1016/j.vacuum.2026.115417

Sharma, D., Bharti, R., Kaushik, P., Sharma, R. and Sutradhar, M., Plant-Assisted Synthesis of $ZrO_2$ Nanoparticles Using Cycas revoluta Extract for Doxycycline Removal from Aqueous Solutions, *Appl. Sci.*, 16(10), 4714 (2026). https://doi.org/10.3390/app16104714

Sharma, G., AlGarni, T. S., Kumar, P. S., Bhogal, S., Kumar, A., Sharma, S., Naushad, M., ALOthman, Z. A. and Stadler, F. J., Utilization of $Ag_2O$–$Al_2O_3$–$ZrO_2$ decorated onto rGO as adsorbent for the removal of Congo red from aqueous solution, *Environ. Res.*, 197, 111179 (2021). https://doi.org/10.1016/j.envres.2021.111179

Sharmiladevi, S., Ramesh, N., Prabhu, S. V and Mayakannan, S., Microwave-assisted functionalized biosorbent preparation using seed gum of Tamarindus indica: characterization and evaluation of Cr(VI) removal potency from tannery effluents, *Biomass Convers. Biorefine.*, 14(12), 13533–13545 (2024). https://doi.org/10.1007/s13399-024-05667-2

Shinde, H. M., Kamble, R. J., Vhanmore, B. D. and Mane, C. B., An innovative fabrication of g-$C_3N_4$-$ZrO_2$ nanocomposite with enhanced photocatalytic degradation of methylene blue under UV–visible light, *J. Opt. (India)*, 55(3), 2304–2318 (2026). https://doi.org/10.1007/s12596-024-02394-9

Shokoohi, R., Salari, M., Safari, R., Zolghadr Nasab, H. and Shanehsaz, S., Modelling and optimisation of catalytic ozonation process assisted by $ZrO_2$-pumice/$H_2O_2$ in the degradation of Rhodamine B dye from aqueous environment, *Int. J. Environ. Anal. Chem.*, 101(15), 2629–2653 (2021). https://doi.org/10.1080/03067319.2019.1704748

Sismanoglu, S. and Buran, E., Azo dye adsorption on $ZrO_2$ and natural organic material doped $ZrO_2$, *Sci. Rep.*, 15(1), 2842 (2025). https://doi.org/10.1038/s41598-024-83639-2

Tahir, S., Waheed, F., Akram, M., Salman, M., Farooq, U., Saleem, S. and Ehsan, A., Vanadium-Doped Zirconia as an Efficient Visible-Light Photocatalyst for Advanced Treatment of Dye-Loaded Wastewater, *Iran. J. Catal.*, 16(2), 222–241 (2026). https://doi.org/10.57647/ijc.2026.1602.15

Varma, V. K. C., Rathinam, R., Suresh, V., Naveen, S., Satishkumar, P., Abdulrahman, I. S., Salman, H. M., Singh, P. and Kumar, J. A., Urban waste water management paradigm evolution: Decentralization, resource recovery, and water reclamation and reuse,

Article in Press

*Environ. Qual. Manage.*, 33(4), 523–540 (2024). https://doi.org/10.1002/tqem.22109

Wahba, M. A. and Yakout, S. M., Microwave-synthesized $ZrO_2$/ZnO heterostructures: fast and high charge separation solar catalysts for dyes-waste degradation, *J. Sol-Gel Sci. Technol.*, 104(2), 330–341 (2022). https://doi.org/10.1007/s10971-022-05936-4

Zhu, Y., Wang, Y. and Yan, X., Preparation of Chitosan-Coated *Toddalia asiatica (L.)* Lam Extract Microcapsules and Its Effect on Coating Antibacterial Properties, *Coat.*, 14(8), 942 (2024a). https://doi.org/10.3390/coatings14080942

Zhu, Y., Wang, Y. and Yan, X., The Effects of Urea–Formaldehyde Resin-Coated *Toddalia asiatica (L.) Lam* Extract Microcapsules on the Properties of Surface Coatings for Poplar Wood, *Coat.*, 14(8), 1011 (2024b). https://doi.org/10.3390/coatings14081011

Article in Press